

31 Abstract

32 Sediment cores recently collected from the Chilean Margin during D/V *JOIDES Resolution*
33 Expedition 379T (JR100) document high- and low-frequency variability in shipboard-generated
34 records of the spectral Green/Blue (G/B) ratio. These changes show a strong coherence with
35 foraminiferal isotope composition, Antarctic ice core records, and sediment lithology (e.g.,
36 higher diatom abundances in greener sediment intervals), suggesting a climate-related control on
37 the G/B ratio. Here, we test the utility of G/B as a proxy for diatom productivity at Sites J1002
38 and J1007 by calibrating G/B to measured biogenic opal. Strong exponential correlations
39 between measured opal content and the G/B ratio were found at both sites. We use the empirical
40 regressions to generate continuous records of opal contents (opal%) on the Chilean Margin.
41 Redox-sensitive sedimentary U/Th generally co-varies with the reconstructed opal% at both
42 sites, supporting the association between sediment color, sedimentary U/Th, and productivity.
43 Lastly, we calculated opal mass accumulation rate (MAR) at Site J1007 over the last ~150,000
44 years. The G/B-derived opal MAR record from Site J1007 largely tracks existing records derived
45 from traditional wet-alkaline digestion from the south and eastern equatorial Pacific Ocean, with
46 a common opal flux peak at ~ 50 ka suggesting that this increased diatom productivity in the
47 eastern equatorial Pacific was likely driven by enhance nutrient supply from the Southern Ocean
48 rather than dust inputs as previously suggested. Collectively, our results identify the G/B ratio as
49 a useful tool with the potential to generate reliable, high-resolution paleoceanographic records
50 that circumvent the traditionally laborious methodology.

51 Plain Language Summary

52 The color of marine sediments often corresponds to oceanic and sedimentary processes that can
53 influence the global climate system. Visual inspection of new sediment cores collected from the
54 Chilean Margin revealed substantial downcore changes in green and blue sediment colors.

55 Greener sediment intervals were usually enriched with diatoms, whereas bluer sediments were
56 rich in clay minerals. A specialized camera was used to scan the cores and enable us to
57 quantitatively describe the core colors using the green/blue ratio. The similarity of the downcore
58 green/blue ratio with Antarctic ice core records suggests that it may serve as a quick tool to
59 estimate the age of the cores during the cruise. In this paper, we show that changes in the
60 green/blue ratio are a function of diatom (biogenic opal) productivity and use a calibrated
61 relationship to calculate a continuous record of opal flux at the Chilean Margin over the last
62 150,000 years. A distinct opal flux maxima at 50,000 years ago is observed, similar to previous
63 studies in the eastern equatorial Pacific. This common event implies a tight link between the
64 high- and low- latitude eastern Pacific Ocean, potentially attributable to enhanced nutrient supply
65 from the Southern Ocean.

66 **1. Introduction**

67 Variations in Southern Ocean and South Pacific primary productivity have been invoked as
68 possible drivers of glacial-interglacial climate change and atmospheric CO₂ variability
69 ([Brzezinski et al., 2002](#); [Matsumoto et al., 2002](#); [Sigman & Boyle, 2000](#); [Toggweiler et al.,](#)
70 [2006](#)). Our understanding of the role primary productivity plays in the climate system on these
71 timescales is partly attributable to records of opal mass accumulation rates (MAR) in marine
72 sediments ([Anderson et al., 2009](#); [Bradtmitter et al., 2007](#); [Charles et al., 1991](#); [Dubois et al.,](#)
73 [2010](#)). Many of the records spanning glacial timescales, however, do not have adequate
74 resolution to resolve (sub)millennial-scale changes, which have been shown to influence both the
75 inception and termination of glacial periods ([Jouzel et al., 2007](#)). This is partly because the
76 traditional wet-alkaline methods that are used to derive these records are laborious (e.g.,

77 [Mortlock & Froelich, 1989](#)), which limits the viability of generating continuous, high-resolution
78 records of opal MAR across glacial-interglacial intervals.

79

80 One potential avenue to circumvent this obstacle and generate high-resolution opal MAR records
81 is by utilizing the color spectrum of marine sediments derived from core image scanning ([Mix et
82 al., 1995](#); [Nederbragt et al., 2000](#)). Generation of sedimentary red-green-blue (RGB) records
83 upon core recovery is standard for most paleoceanographic coring operations and can provide
84 millimeter-scale resolution of sediment properties (e.g., [Mix et al., 1992](#)). These data are often
85 translated to L*, a*, and b* values, which have been widely used for core stratigraphy and
86 paleoceanographic reconstructions (e.g., [Peterson et al. 2000](#)). However, the raw RGB data may
87 be of equal utility since variations in the sediment color often correspond to key oceanic or
88 sediment processes (e.g., primary productivity, terrigenous input, and sediment diagenesis). For
89 example, [Mix et al. \(1992\)](#) documented a close correlation between high Red/Blue ratios and the
90 presence of sulfides in Eastern Equatorial Pacific (EEP) marine sediment, and [Penkrot et al.
91 \(2018\)](#) reported that the Green/Blue ratio closely tracks biogenic opal in sediment cores taken
92 from the Gulf of Alaska. While these are important observations, the established relationships
93 are qualitative. To leverage these high-resolution records for reconstructing regional primary
94 productivity, an empirical relationship between RGB variables (e.g., Green/Blue) and a
95 lithologic component (e.g., biogenic opal) must be established.

96

97 Recent drilling operations on the south Chilean Margin (D/V *JOIDES Resolution* Exp. 379T
98 funded through the NSF *JR100* program) recovered 100-m sediment cores to investigate
99 (sub)millennial-scale to glacial-interglacial variability since the penultimate glaciation. Here, we

100 utilize sites J1002 and J1007 ([Figure 1](#)), which document high-frequency changes in the
101 sediment spectral Green/Blue (G/B) ratio. The G/B data were initially used onboard as a
102 stratigraphic tool owing to similarities with global climate records (e.g., EDML ice core).
103 Shipboard lithologic analyses subsequently revealed that sediments enriched with diatoms
104 coincide with high spectral green values, whereas clay-rich sediments corresponded with high
105 blue values. Thus, G/B records in Chilean Margin cores may serve as a paleoceanographic
106 archive of opal percentage in regional sediments.

107

108 In this paper, we first explore the conceptual background of the proxy itself, as well as the
109 rationale for using G/B in our stratigraphic efforts. We then test the hypothesis that the G/B
110 record correlates with opal content in sediments on the Chilean Margin by calibrating the proxy
111 to biogenic opal concentrations quantified by traditional methods ([Mortlock & Froelich 1989](#)).
112 Lastly, we use the G/B records and initial core stratigraphy based on radiocarbon ages and
113 benthic oxygen isotope records to generate continuous opal MAR records for the last ~150,000
114 years at Site J1007, offering the highest resolution record of diatom productivity in the south
115 Pacific Ocean through most of the last glacial cycle.

116

117 **2. Materials and Methods**

118 2.1 Geological and oceanographic settings

119 Our study region in the southeast Pacific Ocean ranges from the central to south Chilean Margin,
120 where the northward deflection of Antarctic Circumpolar Current (ACC) forms the Peru-Chile
121 Current (PCC, a.k.a Humboldt Current) between 40°S-45°S ([Strub et al., 1998](#)). The northward
122 flowing PCC dominates the surface circulation pattern along the west coast of South America

123 (Figure 1). The poleward flowing Gunther Undercurrent underlies the PCC between 100-400 m
124 water depth (Hebbeln et al., 2000; Strub et al., 1998). Between 500-1200 m water depth flows
125 Antarctic Intermediate Water (AAIW), which forms today at the Subpolar Front by mixing cold,
126 fresh Polar Front waters with Subantarctic Mode Water (Piola and Georgi 1982; Sallée et al.
127 2010; Sloyan and Rintoul, 2001). Beneath AAIW sits the northern flowing Antarctic Bottom
128 Water and sluggish Pacific Deep Water (PDW) return flow, which enters the Southern Ocean at
129 mid-depths (Talley, 2013). Coastal upwelling is intensive throughout the year north of 35°S but
130 is restricted to late spring and early fall between 35°S-42°S. South of 42°S, coastal upwelling is
131 inhibited by the prevailing southern westerly winds (Strub et al., 1998).

132

133 The current oceanographic regime makes the Chilean Margin a remarkably productive region in
134 the modern setting. Annual chlorophyll concentration in surface waters along the Chilean Margin
135 reaches up to 4 mg/m³ (Figure 1b). Annual primary productivity in this region is dominated by
136 diatoms (Abrantes et al., 2007), and based on satellite-measured pigments is estimated to about
137 ~150 gC/m²/yr off central Chile (31°S-37°S) and ~60 gC/m²/yr along the south Chilean Margin
138 (i.e., south of 37°S; Antoine and Morel, 1996). The latitudinal distribution pattern of opal
139 contents (opal%) and organic carbon contents (C_{org}%) in surface sediment samples reflect the
140 overlying pigment concentration; surface sediment opal% ranges from ~5% off central Chile to
141 ~3% in the south (Romero and Hebbeln, 2003). Despite the high diatom productivity in this
142 region, the opal percentages in the sediments are very low because of the extremely high
143 sedimentation rates on the margin, which can exceed 200 cm/kyr (Hebbeln et al., 2007). High
144 sedimentation rates along the Chilean Margin are largely attributable to significant regional
145 precipitation and high elevations of the Coastal Range and the Andes. Precipitation can vary

146 from <1000 mm/yr in central Chile to >2500 mm/yr south of 40°S, leading to increased
147 terrigenous supply in the south (Stuut et al., 2006).

148

149 2.2 Study sites

150 Sites J1002 and J1007 were recovered from the Chilean Margin using the D/V *JOIDES*
151 *Resolution* drilling platform during Expedition 379T in Summer 2019 (Figure 1). Site J1002 (46°
152 4.2964'S, 75° 41.2300'W) is located on the south Chilean Margin offshore Northern Patagonia
153 on a bench in the continental slope at a water depth of 1534 m. At present, this site lies under the
154 northern extent of the ACC and is bathed in PDW. Site J1007 (36° 32.5400'S, 73° 39.9900'W) is
155 located on the continental crust 60 km shoreward of the Chile Trench. With a water depth of 808
156 m, Site J1007 lies in the heart of modern AAIW (Bova et al., 2021).

157

158 2.3 Age models

159 Age models for Site J1002 and J1007 (Figure S2, S3; see age control points in Table S3) were
160 based on a combination of AMS radiocarbon dating and the visual correlation to the LR04
161 benthic stack (Lisiecki and Raymo, 2005). Calendar ages for the upper parts of the core are
162 based on AMS ¹⁴C dating of planktonic foraminifera (*Globigerina bulloides*): eight in the upper
163 67 m of Site J1002 and seven in the upper 23 m at Site J1007, with calendar corrections using
164 IntCal20 (Reimer et al., 2020; Figure 3). Below these depths, stratigraphy is based on visual
165 correlation between benthic foraminifer *Uvigerina spp.* $\delta^{18}\text{O}$ and the LR04 benthic stack. The
166 *Undatable* program has been used to refine the original age models (Lougheed et al., 2019),
167 improving the resolution and precision of the opal flux estimate simultaneously (See age-depth
168 figures in Figure S1). Comparison with benthic $\delta^{18}\text{O}$ from the nearby ODP Site 1234 (36°14'S,

169 73°41'W, 1015 m; [de Bar et al., 2018](#); [Heusser et al., 2006](#); [Robinson et al., 2007](#)) is further
170 applied to constrain the J1007 age model. Nonetheless, we note that the J1007 age model below
171 66 m is loosely constrained due to limited resolution of the benthic $\delta^{18}\text{O}$ record. For J1007, the
172 interval between 82 m to 86 m is thought to represent the light $\delta^{18}\text{O}$ “plateau” of Marine Isotope
173 Stage (MIS) 5e. However, the $\delta^{18}\text{O}$ of this recognized MIS 5e stage are not significantly more
174 depleted than the Holocene as might be expected. Therefore, we caution that it is possible that
175 the real MIS 5e “plateau” was missed due to low sampling resolution and the bottom of J1007
176 does not reach MIS 5e. This uncertainty has, however, no bearings on the discussion and
177 conclusion of the paper but should be noted by potential users of the core data.

178

179 2.4 Spectral G/B ratio

180 Although extremely high sedimentation rates along the southern Chilean Margin offer the
181 opportunity to generate high-resolution paleoproductivity records, they also pose a few
182 challenges. First, the concentration of biogenic components (e.g., organic carbon% and opal%)
183 are very low, approaching the detection limits of the analytical methods. And secondly, taking
184 advantage of the high sedimentation rates for generation of high-resolution records using
185 traditional methods is laborious and practically unattainable. Therefore, continuous methods can
186 offer valuable information that cannot be obtained from discrete measurements. The advantage
187 of such a method is more in capturing the temporal variability at high resolution than in
188 providing accurate concentrations. The spectral G/B ratio is a quantitative method to describe
189 sediment color in the wavelengths of green and blue ranges. Shipboard color reflectance
190 spectrophotometry was measured on the archive halves of the core using a line-scan camera on
191 the automated Section Half Imaging Logger (SHIL). Sediment cores were scraped using a glass

192 slide after splitting, and the cleaned flat face of the archive half was immediately imaged to
193 prevent color degradation at a resolution of 10 lines/mm. Data were presented as color
194 reflectance parameters of red, green, and blue (Bova et al., 2021). The spectral G/B ratio was
195 calculated as the green parameter divided by the blue parameter.

196

197 Preliminary results of the shipboard smear slide description suggest a possible link between
198 sediment color and lithology, in agreement with previous work (e.g., Mix et al. 1992; Mix et al.
199 1995; Nederbragt et al. 2000; Penkrot et al. 2018). Elevated abundance of diatoms is typically
200 found in greener sedimentary intervals (Figure 2). Similar latitudinal distribution patterns of
201 opal%, C_{org}%, and pigment concentrations suggest that diatoms are the dominant group of
202 primary producers along the Chilean Margin (Abrantes et al., 2007; Romero and Hebbeln, 2003;
203 Stuut et al., 2006). The primary pigments of diatoms are the green chlorophyll-*a* and the blue-
204 green chlorophyll-*c* (Kuczynska et al., 2015; Stauber and Jeffrey et al., 1988). Although
205 chlorophyll can be degraded, most of the breakdown products (e.g., chlorins) are still detectable
206 by regular spectrophotometric methods (Ruess, 2005). Indeed, downcore pigment records have
207 been used to reconstruct productivity changes in lakes and estuaries for decades (Ruess et al.,
208 2005; Ruess et al., 2013). Thus, it has been hypothesized that the spectral color of green is
209 mainly produced by diatom-related pigments in this region. In contrast, cores with a dominance
210 of siliciclastic components and a lower abundance of diatoms are usually found to be bluer
211 (Figure 2). Considering the tremendous terrestrial input commonly found along the Chilean
212 Margin, the siliciclastic component likely produces the blue spectral color. We therefore
213 hypothesize that the spectral G/B ratio reflects the relative abundance of biogenic silica in

214 sediments, and based on our calibration, can use it as to quantify diatom productivity along the
215 Chilean Margin over time.

216

217 Given the high-temporal variability of the records, the spectral G/B ratio has also been a useful
218 tool for stratigraphic correlations among holes drilled during Expedition 379T because it is likely
219 linked to regional climate processes (Bova et al., 2021). Previous studies suggest that Antarctic
220 climate changes have a significant impact on surface water dynamics and terrestrial input off of
221 the coast of Chile (Lamy et al., 2004; Kaiser et al., 2007). Regional surface water processes are
222 closely linked to diatom production, hence the spectral green parameter of the sediments. On the
223 other hand, the terrestrial input is assumed to contribute to the spectral blue parameter in
224 sediments. The variation of spectral G/B ratio may be sensitive to climate dynamics, making it
225 applicable for stratigraphic correlations. To validate these assumptions, we compare the
226 downcore variations in G/B at J1002 and J1007 with the benthic foraminiferal $\delta^{18}\text{O}$ record at
227 each site. The remarkable consistency between the G/B and benthic $\delta^{18}\text{O}$ at both sites validates
228 the use of the G/B ratio for stratigraphic correlations along the Chilean Margin (Figure 3).

229 Moreover, G/B ratios at both sites show good correlations with Antarctic ice core $\delta^{18}\text{O}$ records,
230 with higher G/B values usually corresponding to warm intervals near Antarctica and lower G/B
231 values corresponding with cold intervals; this observation further demonstrates its utility for
232 stratigraphic correlations (Figure 3). This tool has been especially useful for shipboard
233 correlation as other sedimentary property records in these regions (e.g., magnetic susceptibility,
234 natural gamma radiation, and other color properties) had muted signals. For example, magnetic
235 susceptibility was widely used for shipboard correlation among holes, but for high sedimentation
236 rate sites—especially those with thick Holocene section that were devoid of any appreciable

237 magnetic susceptibility signal—G/B ratios turned out to be the most applicable stratigraphy tool
238 ([Bova et al., 2021](#)).

239

240 2.5 Biogenic opal analyses

241 J1002 and J1007 were sampled at intervals spanning the range of G/B values measured at each
242 site to investigate the relationship between opal% and G/B. Biogenic silica concentrations were
243 measured by conventional wet-alkaline digestion, including mineral correction procedures
244 modified after [Conley et al. \(2001\)](#). The mineral correction was critical for sediments with
245 relatively low biogenic silica contents as it minimizes the effect of mineral silicates. A total of 22
246 samples from J1002 and 41 samples from J1007 were analyzed. About 250 mg of freeze-dried
247 sediments were homogenized using a mortar and pestle and digested by 1 mol/L Na₂CO₃
248 solution in an 80°C water bath. The tubes were shaken quickly for complete digestion every 20
249 minutes. Subsamples of 1 mL were taken after 3, 4, and 5 hours of digestion time. Silicate
250 concentration of each subsample was measured by molybdate blue spectrophotometric
251 measurements using an Agilent Cary 60 UV-Vis Spectrophotometer at Rutgers University
252 peaked at 812 nm, modified after [Mortlock and Froelich \(1989\)](#) (see detailed experimental and
253 data-processing procedure in [Text S1](#)). Ideally, a linear regression was made with the three
254 subsamples, with extrapolation to the intercept providing the final biogenic silica concentration
255 ([DeMaster, 1979](#)). Finally, opal% was calculated as biogenic silica concentration multiplied by
256 2.4 ([Mortlock and Froelich, 1989](#)). The standard error of our measurements was 0.35% based on
257 14 duplicate measurements. Wet-alkaline digestion could be affected by "noise" from clay
258 ([Conley et al., 2001](#)). Our mineral correction protocol suggests, however, that clay only

259 contributes to a stable background noise of 0.3% ([Figure S1](#)), which was then removed during
260 the data-processing procedure.

261
262 2.6 Quantifying U and Th contents with shipboard natural gamma radiation data
263 Full natural gamma radiation (NGR) data for Site J1002 and J1007 were collected during
264 Expedition 379T. Original NGR spectra obtained on board were composed of numerous peaks
265 for the ^{238}U and ^{232}Th series. Thus, sedimentary contents of thorium (^{232}Th), and uranium (^{238}U)
266 were estimated by identifying and quantifying their characteristic energy peaks using a
267 MATLAB algorithm by [De Vleeschouwer et al. \(2017\)](#).

268

269 **3. Results and Discussions**

270 3.1 Calibration of spectral G/B with measured opal%
271 Shipboard spectral G/B records exhibit a generally northward increasing trend along the Chilean
272 Margin, in agreement with annual chlorophyll distribution in surface waters ([Figure 1b](#)). In
273 addition to lower average values, the G/B for Site J1002 also shows smaller variabilities than
274 J1007. Measured opal% for Site J1002 and Site J1007 vary between 0.36-4.36% and 1.89-
275 5.35%, respectively. In general, measured opal% covary with the G/B, with higher measured
276 opal% usually found in greener sediments ([Figure 4a](#)). Eight samples from J1007 and one sample
277 from J1002, however, apparently underestimate opal% with respect to G/B ([Table S2](#)). In all
278 cases these intervals are associated with prominent low values of magnetic susceptibility ([Figure](#)
279 [5](#)), which hints to the possibility of diagenetic overprints.

280

281 At Site J1007, the organic carbon percentage ($C_{org}\%$) correlates well with measured opal%
282 ($n=21$, $r^2=0.51$, $p<0.05$; [Figure 4b](#)), in agreement with the robust correlation between opal% and
283 $C_{org}\%$ in the nearby surface sediments ([Romero and Hebbeln, 2003](#)). Those samples with
284 potentially underestimated opal%, within low magnetic susceptibility intervals, are similarly
285 offset from the expected values based on average correlation between opal% and $C_{org}\%$.
286 Preliminary shipboard analysis shows the frequent presence of nannofossils and diatoms in
287 sediments along the Chilean Margin ([Bova et al., 2021](#)). Combining downcore and surface
288 sediment records, it can be deduced that primary productivity in this area is dominated by
289 diatomaceous species, with carbonate nannofossil species as a minor contributor. In contrast,
290 $C_{org}\%$ shows only a weak correlation with G/B ([Figure 4c](#)), which suggests one or both
291 indicators are impacted by degradation. As most degradation products of chlorophyll retain their
292 original color ([Ruess, 2005](#)), it is likely the G/B proxy is a more robust indicator and possibly
293 independent of organic matter preservation. Nonetheless, with these caveats in mind, data from
294 low magnetic susceptibility intervals should be considered with higher uncertainty.

295
296 Excluding the underestimated data points (20% of entire data set, shown in figure 5), strong
297 exponential correlations are found between G/B and measured opal% at both sites (J1002:
298 $\ln(y)=5.8x-6.3$, $n=14$, $r^2=0.73$, $p<0.05$; J1007: $\ln(y)=5.8x-5.5$, $n=22$, $r^2=0.48$, $p<0.05$; where x
299 and y are G/B values and opal%; [Figure 4a](#)). The calibrations of J1002 and J1007 show the same
300 slope but different intercept, indicating similar sensitivity of G/B and differences in background
301 colors. Root mean square deviation (RMSD) were calculated based on the differences between
302 measured opal% and the reconstructed opal% derived from G/B values. The RMSD is 0.68% for
303 J1002 and 0.72% for J1007, reflecting the uncertainty of regression models in this study.

304

305 Note that while the relationships between G/B, opal%, and C_{org}% are robust, the empirical
306 calibrations are site-specific to J1002 and J1007 and cannot be transferred to other sites, even
307 those in the same region. We hypothesize that variable clay mineralogies along the meridional
308 transect (e.g., [Lamy et al., 1998](#)) cause spatial differences in the total "blue" content in the
309 sediments, which were presented by different intercepts of the calibration equations. Similar to
310 X-ray fluorescence (XRF) scanning records of cores, the G/B ratio may also provide a semi-
311 quantitative record that will require a site-specific calibration at each site to convert the relative
312 changes to a record of opal%. It is noteworthy, however, that the two studied sites represent an
313 extreme case where the opal concentrations are very low due to dilution from the very high
314 sedimentation rates. It is likely that the method and calibration would be more robust in sites
315 where the contribution of clays and sedimentation rates are lower than those encountered on the
316 Chilean Margin.

317

318 3.2 Reconstructing opal% records

319 Having established the G/B proxy as a tracer of opal% at our study sites, we now use the
320 exponential regression equations above to reconstruct past changes of opal% from the G/B
321 records. Downcore opal% ranges between 0.6-2.5% and 1.6-8.8% for J1002 and J1007,
322 respectively ([Figure 5](#)). Reconstructed opal% shows relatively large-scale variability at Site
323 J1007, with the highest opal% for the past 150 kyr found during Termination II and MIS 3
324 ([Figure 5a](#)). At Site J1002, reconstructed opal% shows a prominent peak during Holocene, but
325 remains low and stable before Last Glacial Maximum (LGM, 23-19 ka) ([Figure 5b](#)). At Site
326 J1002, opal% only ranges ~1% before the LGM, which can be almost entirely attributed to

327 reconstruction uncertainty ($2 \times \text{RMSD} = 1.36\%$, see pink shading in [Figure 5](#)). Thus, we caution
328 against the utility of the J1002 opal% reconstruction before the LGM and do not use it for
329 paleoceanographic interpretation.

330
331 Over the past 30 kyr, opal% at J1007 and J1002 gradually increases from the last glacial period
332 to the Holocene. During the late Holocene, J1007 opal% is 4-5%, similar to the opal content of
333 ~5% in nearby surface sediments ([Romero and Hebbeln, 2003](#)). Meanwhile, J1002 opal% of
334 about 2.5% during the Holocene agrees with opal contents of ~4% in surface sediments at 44°S
335 ([Chase et al., 2015](#); [Romero and Hebbeln, 2003](#)). The opal% range for J1007 over the last 30 kyr
336 (2-6%) is similar to that of two nearby sites, and the variation trend mimics GeoB 3395-3. At
337 Site J1002, the low opal% prior to the last glacial period is attributable to a marked increase in
338 sedimentation rate (>3 m/kyr), which appears to significantly dilute the opal% relative to the
339 Holocene.

340
341 Previous opal% reconstructions along the Chilean Margin only covered the past 30 kyr, and most
342 vary in a similar range but with different patterns. On the central Chilean Margin, site GeoB
343 3395-3 (35°13'S, 72°48.5'W, 678 m) has opal% ranging from ~1.5-5% for the past 23 kyr, with
344 the highest values appearing during late Holocene ([Romero and Hebbeln, 2003](#); [Romero et al.,](#)
345 [2006](#)). The opal% at ODP Site 1234 (36°14'S, 73°41'W, 1015 m) range from ~2-5% for the last
346 30 kyr, with peak values occurring during the last glacial period (26-20 ka), but slightly before
347 LGM ([Chase et al., 2014](#)). Moreover, it is worth noting that the chlorins content at nearby site
348 GeoB 7165-1 (36°33'S, 73° 40'W, 797 m) also increases from the LGM to late Holocene
349 ([Mohtadi et al., 2008](#)). Further south, the diatom abundance record from ODP Site 1233 (41°S,

350 74°27'W, 838 m) is very similar to that of ODP 1234 (Chase et al., 2014). Overall, the consistent
351 range of reconstructed opal% at J1002 and J1007 with nearby sites strongly support the
352 robustness of spectral G/B-opal% proxy.

353

354 3.3 Sedimentary U/Th

355 In nature, thorium occurs almost entirely as ^{232}Th while uranium primarily exists as ^{238}U , both of
356 which are primarily supplied to the oceans by riverine runoff (McManus et al., 2006). As a non-
357 redox-sensitive metal, ^{232}Th has low solubility in rivers and oceans, and is largely absorbed on
358 the surface of clay minerals (Harmsen et al., 1980). On the other hand, ^{238}U exist as both soluble
359 U(VI) and insoluble U(IV) phases (Langmuir, 1978). In oxygenated seawater, ^{238}U is present
360 dominantly as a stable U(VI) carbonate complex, with a small fraction associated with
361 particulate organic carbon flux (McManus et al., 2005). Under suboxic conditions, authigenic U
362 accumulates in the sediments as a combination of the bio-authigenic phase associated with
363 settling organic particles and that formed by diffusion of U into sedimentary pore waters (Barnes
364 and Cochran, 1990; Henderson and Anderson, 1999; McManus et al., 2005). Therefore,
365 sedimentary U/Th, which minimizes the influence of variable detrital sources and sedimentation
366 rates (thus the authigenic U burial rate), can be used as a non-quantitative indicator of redox
367 conditions of the sediments.

368

369 Both the thorium and uranium contents are higher at Site J1002 than Site J1007, corresponding
370 to larger terrestrial input to the south Chilean Margin. In contrast, U/Th at Site J1007 was found
371 to be higher than that of J1002 (Figure 5). Higher U/Th reflects more suboxic sedimentary
372 conditions (referring to low dissolved oxygen availability in bottom waters), high organic carbon

373 rain rates, or some combination of both processes (McManus et al., 2006). We observe marked
374 similarities in both trends and magnitudes between measured opal%, G/B-reconstructed opal%,
375 and U/Th profiles at both sites (Figure 5). The co-occurrence of high productivity intervals (high
376 opal %, high G/B) and suboxic conditions, as indicated by high U/Th, supports the use of G/B as
377 a proxy of diatom productivity on the Chilean Margin.

378

379 3.4 Reconstructed opal MAR

380 Previous studies along the Chilean Margin provide only short and relatively low-resolution
381 records of opal MAR (Chase et al., 2014; Hebbeln et al., 2002; Mohtadi et al., 2004; Romero et
382 al., 2006). To fill the research gap on sub-orbital-scale variability in diatom productivity, we
383 generated opal MAR records with G/B-derived opal% from Site J1007. Opal MAR was
384 calculated as:

$$385 \text{Opal MAR} = \text{opal\%} * \rho_{\text{dry}} * \text{LSR} \quad (\text{Eq. 1})$$

386 where the opal% is calculated from the calibrated spectral G/B ratio, ρ_{dry} is the shipboard-
387 measured dry bulk density of the sediment (g/cm^3), and LSR is the linear sedimentation rate
388 (cm/kyr) as established by J1007 age model.

389

390 In general, the sedimentary record of opal MAR shows large-amplitude variation at Site J1007
391 (Figure 6). Over the last 30 kyr, opal MAR of 2-3 $\text{g}/\text{cm}^2/\text{kyr}$ were found before the LGM, which
392 decreased to $\sim 1 \text{ g}/\text{cm}^2/\text{kyr}$ during the deglaciation and into the Holocene. The opal flux records
393 from two adjacent sites (GeoB 3395-3 and ODP Site 1234) show a distinct peak of ~ 1.5
394 $\text{g}/\text{cm}^2/\text{kyr}$ during the LGM (Figure 6a; Chase et al., 2014; Romero et al., 2006). Further south,

395 opal MAR from ODP Site 1233 reaches a peak during the last glacial period (1.8 g/cm²/kyr) and
396 decreases below 0.2 g/cm²/kyr since 20 ka (Chase et al., 2014). Note that ²³⁰Th normalization
397 was applied to opal MAR calculations at ODP Site 1234 and ODP Site 1233, but not at GeoB
398 3395-3. The opal MAR variation of Site J1007 shows higher levels with longer duration than
399 observed at the other three nearby sites. The difference may be due to the difference in the data
400 sources. The J1007 record is based on continuous high-resolution G/B ratio, whereas the other
401 records are based on low-resolution discrete wet analyses (Figure 5). In fact, comparing the latter
402 with our discrete samples from J1007 suggests a greater consistency among the record in terms
403 of regional changes in opal productivity. We note, however, that changes in sedimentation rate at
404 Site J1007 impart the largest influence on the opal MAR, and the broad peak reflects this.

405
406 On a longer timescale, the most outstanding features of the Site J1007 opal MAR record are two
407 large peaks, one at ~50 ka and a secondary peak that we tentatively place at Termination II based
408 on benthic $\delta^{18}\text{O}$ tuning (Figure 3; Figure 6b). Similar opal flux maxima during MIS 3 have been
409 documented at the site of V19-30 (Figure 6b) and other sites in the EEP (e.g., TR163-31, ME-24)
410 (Dubois et al., 2010; Kienast et al., 2007; Hayes et al., 2011). These opal MAR changes along
411 the eastern Pacific basin are further echoed by a Diol index record offshore Southeastern
412 Australia, which infers maximum *Proboscia* diatom abundance during MIS stages 1, 3 and 5e
413 (Lopes dos Santos et al., 2012).

414
415 Enhanced opal preservation related to EEP dust flux (Dubois et al., 2010) and increased
416 contribution of northern hemisphere waters with higher Si:N (Hayes et al., 2011; Kienast et al.,
417 2007) have been discussed as possible drivers for the 50 ka flux peak in the EEP. However, our

418 new opal MAR record from the mid-latitudes clearly refute both the EEP dust controlled or
419 Northern Hemisphere-sourced mechanisms. This common 50 ka event along the eastern Pacific
420 meridional transect, paired with a peak diatom productivity offshore Southeastern Australia,
421 implies a climatic connection between the high and low latitudes in the Southern Hemisphere,
422 likely through nutrient-rich intermediate waters exported from the Pacific-sector of the Southern
423 Ocean (Talley, 2013). Southern Ocean Intermediate Waters supply nitrogen, phosphorous, and
424 silicate to the global thermocline, thereby supporting up to 75% of tropical production (Ayers et
425 al., 2013; Sarmiento et al., 2004). The widely presented MIS 3 opal flux peak supports the idea
426 of enhanced Si supply to low latitudes (Hayes et al., 2011), depicting a clear route of “oceanic
427 tunneling” between the Antarctic and the equatorial Pacific (Pena et al., 2008; Spero and Lea,
428 2002). Moreover, the opal flux at Site J1007 is nearly ten times greater than that of EEP records,
429 implying that mid-latitude continental margins could have served as an important sink for
430 leaking Si from the glacial Southern Ocean (Bradt Miller et al., 2009).

431

432 **4. Conclusions**

433 Diatom production plays a major role in the biological pump, especially in the Southern Ocean
434 and upwelling regions such as along the EEP and western margins of South America.
435 However, because measuring opal% in sediment is analytically very laborious, obtaining high
436 resolution sedimentary records of opal accumulation is practically impossible, especially in cores
437 with very high-sedimentation rates like those along the Chilean Margin. This study demonstrates
438 that using shipboard measurements of the spectral G/B ratio from newly recovered sediment
439 cores on the Chilean Margin, coupled with calibration of discrete samples using traditional
440 methods, can offer a new approach to generate high-resolution paleoceanographic records for

441 reconstructing glacial-interglacial changes in South Pacific diatom productivity. In more detail,
442 we conclude the following:

- 443 1. The spectral green/blue (G/B) ratio in Chilean Margin sediments can serve as an efficient
444 shipboard stratigraphic tool, where other shipboard data (e.g., magnetic susceptibility) are
445 not conclusive.
- 446 2. The G/B records provide high-resolution proxy records for regional changes in diatom
447 productivity over time. The conversion of G/B data to opal% records requires site-specific
448 calibrations from discrete opal% analysis using traditional wet-alkaline digestive methods.
449 Offsets among sites in the G/B ratio to opal% relationships are likely related to lithological
450 effects. Nevertheless, the records suggest that, despite diagenetic effects on biogenic silica
451 and organic matter preservation, the G/B records may more reliably record
452 paleoproductivity, especially in very high sedimentation rates environments where their
453 concentration are diluted.
- 454 3. Continuous records of opal mass accumulation rate on the Chilean Margin over the last
455 ~150,000 years largely tracks existing records from the EEP, with a common opal flux peak
456 at ~50 ka. This suggests a climatic link between high and low latitudes in the South Pacific
457 through intermediate waters.

458

Core Name	Latitude	Longitude	Water Depth (m)	Reference
J1002	46° 4.30'	75° 41.23'W	1534	This study
J1007	36° 32.54'	73° 39.99'W	808	This study
ODP Site 1233	41°S	74°27'W	838	Chase et al, 2014
ODP Site 1234	36°14'S	73°41'W	1051	Chase et al, 2014
GeoB 3395-3	35°13'S	72°48.5'W	678	Romero et al., 2006
V19-30	3°22.98'	83°31.02'W	3091	Hayes et al., 2011

459

460

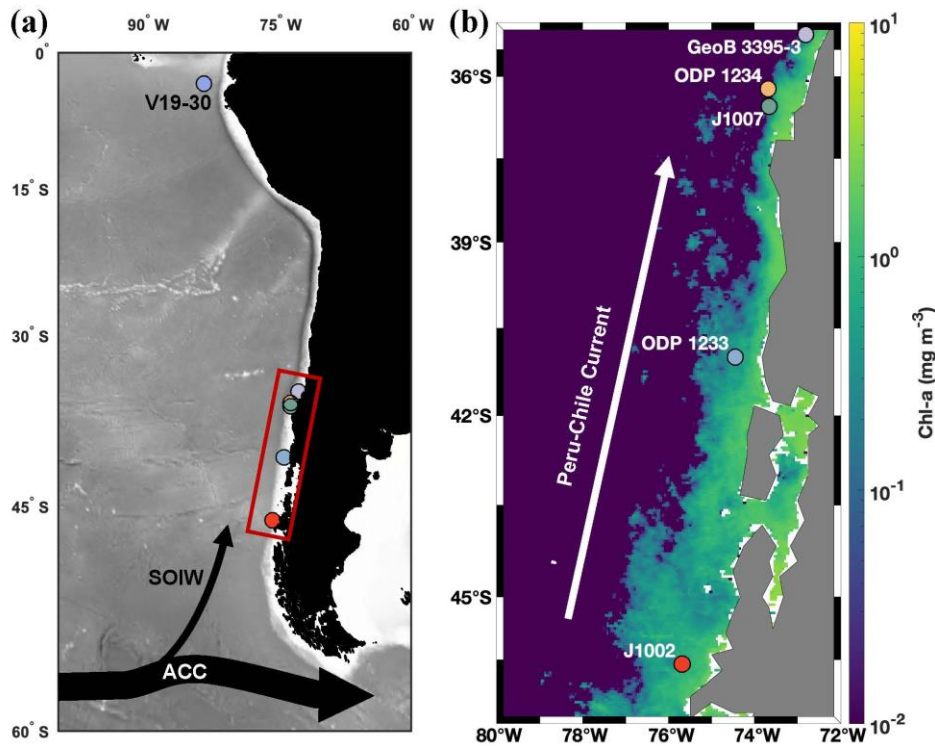
Table 1. Site locations in Figure 1

461

462 **FIGURES AND CAPTIONS**

463

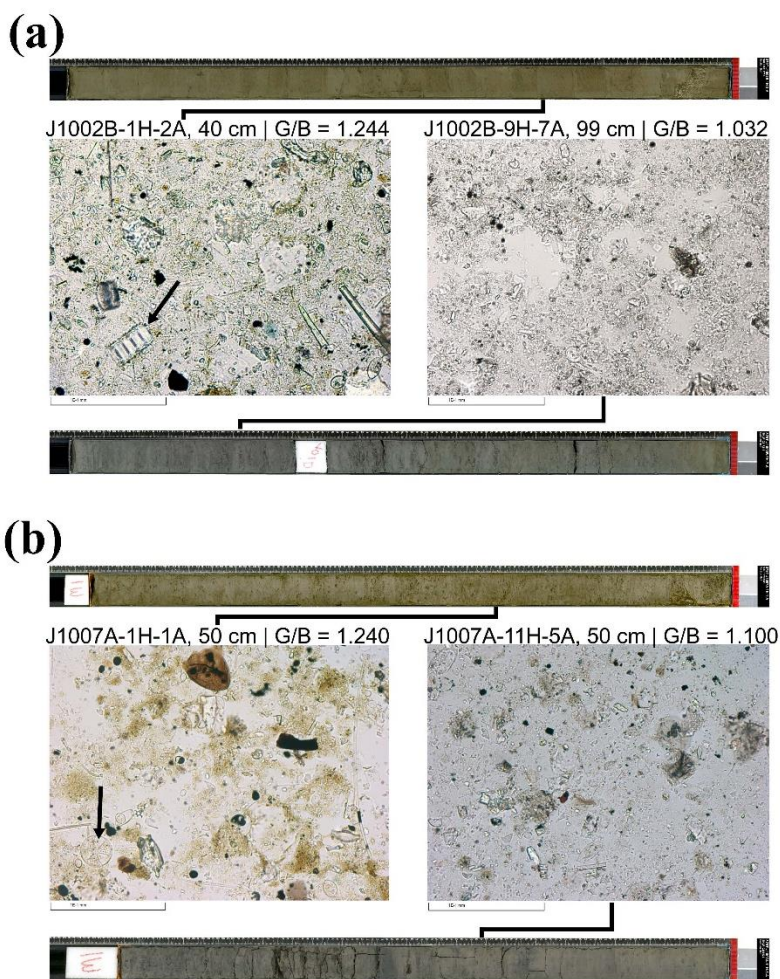
464 **Figure 1.** Map of the South Pacific and study region. A. Core locations of J1002, J1007, and
465 other sites discussed in this paper (Table 1). Black arrows show the path of the Southern Ocean
466 Intermediate Water, the surface flow of the Antarctic Circumpolar Current, and the Peru-Chile
467 Current. B. Zoomed-in view of the Chilean Margin (red box in A), with core locations
468 superimposed on mean annual sea-surface chlorophyll-a concentration. J1002 (red), ODP Site
469 1233 (light blue), J1007 (green), ODP Site 1234 (orange), and GeoB 3395-3 (light purple) are
470 shown. Chlorophyll-a data are from the MODIS-Aqua Level 3 database.



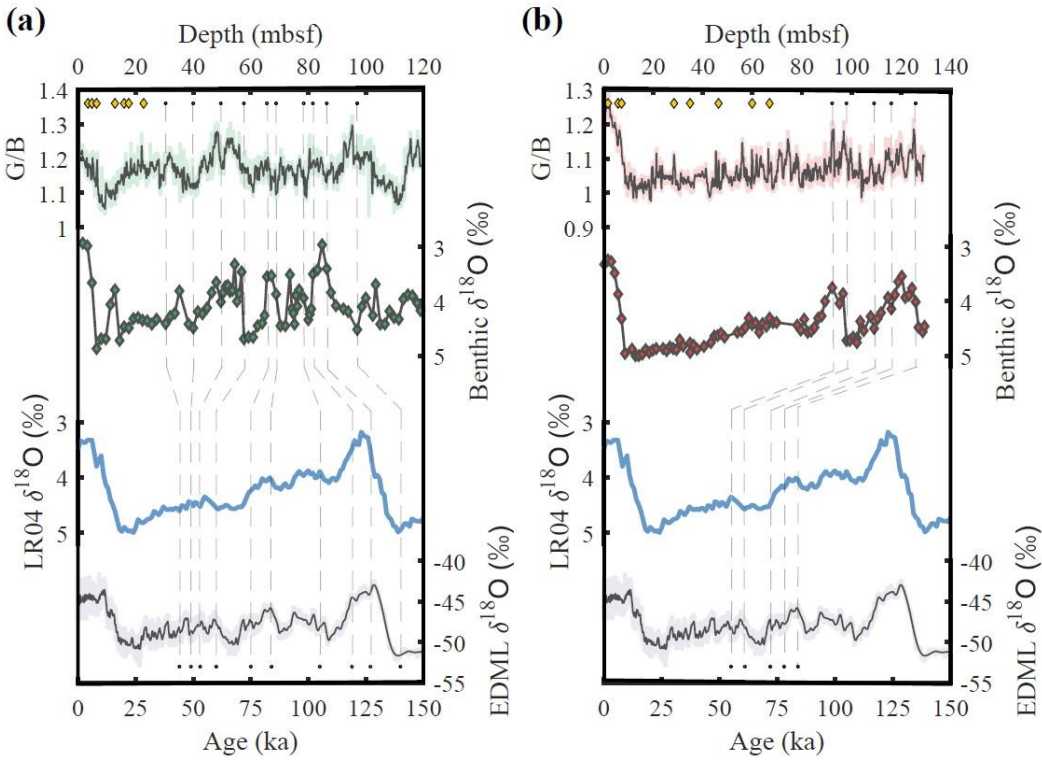
471

472

473 **Figure 2.** Core photos and smear slide photos representing intervals with high and low G/B
474 values Site J1002 (A) and Site J1007 (B). Core photos were taken by line-scan camera on SHIL
475 and smear slide photos under microscope during Expedition 379T. Greener sedimentary intervals
476 (top core sections in both panels) and bluer sedimentary intervals (bottom core sections in both
477 panels) for each site are evident from visual inspection. In both A and B, smear slide photos in
478 the left panels show intervals with abundant diatom presence, corresponding to greener
479 sedimentary intervals, whereas the right panel smear slide images reflect low diatom abundance
480 intervals from bluer intervals. Black arrows show typical diatoms observed in smear slides.

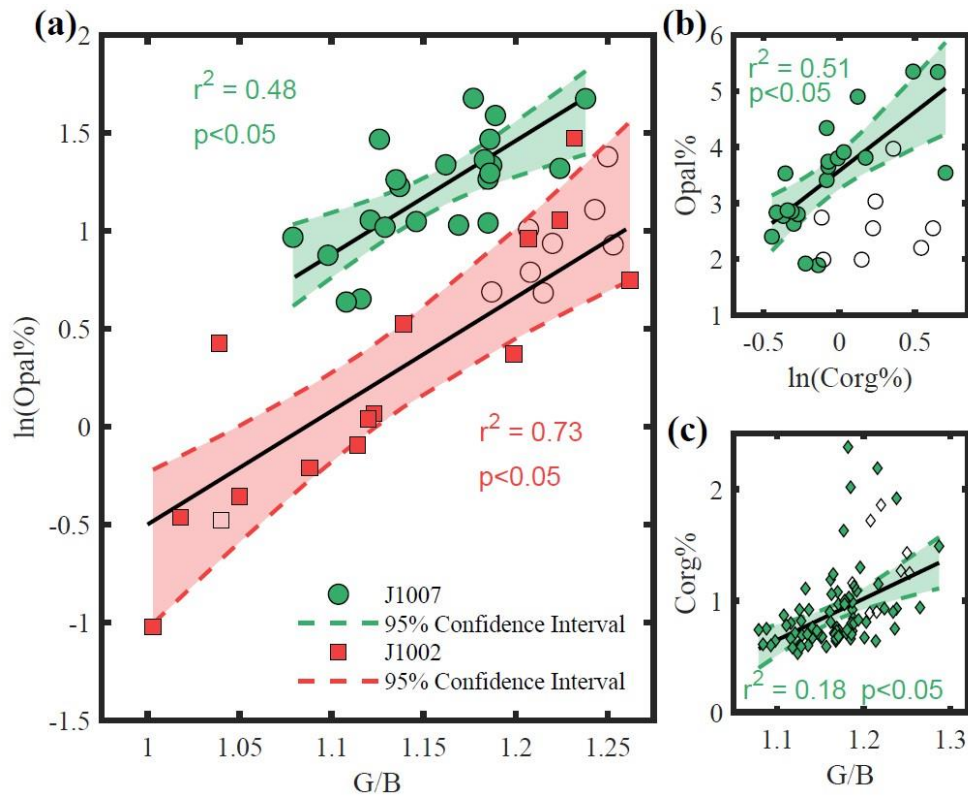


482 **Figure 3.** Stratigraphic correlations between Antarctic ice core $\delta^{18}\text{O}$ (EDML, [EPICA](#)
 483 [Community Members, 2006](#)), LR04 benthic stack ([Lisiecki and Raymo, 2005](#)), the G/B, and
 484 benthic $\delta^{18}\text{O}$ for Site J1007 (A) and Site J1002 (B). Age control points from ^{14}C ages are
 485 displayed (yellow diamonds). Tie points for visual correlation between benthic $\delta^{18}\text{O}$ and LR04
 486 are denoted by vertical dashed lines.



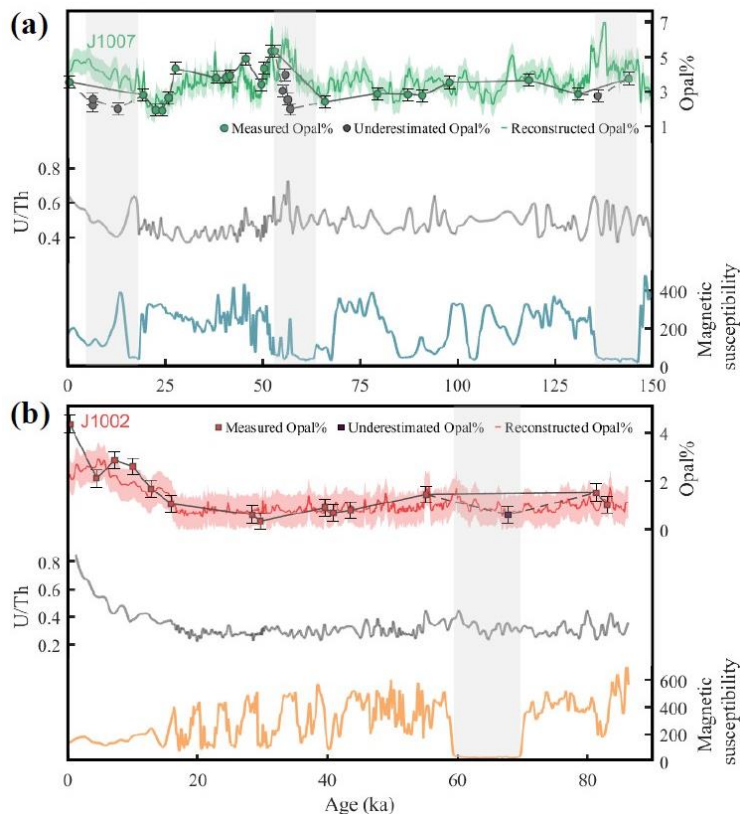
487
 488
 489

490 **Figure 4.** Calibration of the G/B proxy. A. Correlation between opal% and the spectral G/B ratio
491 for Site J1002 (red squares) and Site J1007 (green circles). B. Correlation between opal% and
492 $C_{org}\%$ for Site J1007. C. Correlation between $C_{org}\%$ and spectral G/B ratio for Site J1007. Open
493 symbols in all panels represent potentially underestimated opal% data points from low magnetic
494 susceptibility intervals. Shaded areas represent the 95% confidence interval for each regression.

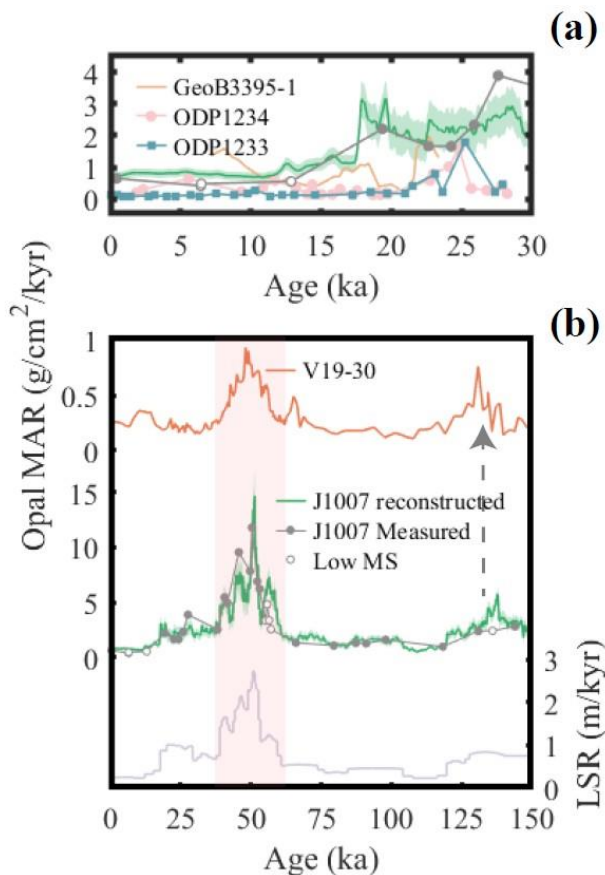


495
496
497

498 **Figure 5.** Downcore opal%, U/Th, and magnetic susceptibility records for Site J1007 (A) and
499 Site J1002 (B). Reconstructed opal% for the last ~150 ka at J1007 (green) and 90 ka at J1002
500 (red) are shown as smoothed solid curves (MATLAB loess smoothing, window = 50) with the ± 1
501 RMSD envelope. Measured opal% (green circles for J1007, red squares for J1002) are
502 superimposed on each reconstructed record. Grey symbols represented potentially
503 underestimated opal% data points from low magnetic susceptibility intervals. The standard error
504 of opal% measurements (0.35%, based on 14 duplicate measurements) was shown as error bar on
505 each data point. Note that we reject those from the calibrations but this does not affect our
506 interpretations of the G/B records. U/Th records are presented as solid grey lines. Magnetic
507 susceptibility at Site J1007 (blue) and Site J1002 (orange) are shown as smoothed solid curves
508 (MATLAB loess smoothing, window = 50). Vertical grey bars denote intervals of low MS
509 coinciding with underestimated opal% data at each site.



511 **Figure 6.** Downcore opal MAR records from the eastern Pacific Ocean. A. Opal MAR variation
 512 for the last 30 ka at GeoB3395-3 (yellow; Romero et al., 2006), ODP Site 1234 (pink; Chase et
 513 al., 2014), and ODP Site 1233 (blue; Chase et al., 2014). Site J1007 (green) opal MAR are
 514 shown as smoothed solid curves (MATLAB loess smoothing, window = 50) with the ± 1
 515 uncertainty envelope (by error propagation from 1 RMSD). Grey markers show opal MAR
 516 calculated from measured opal% (closed circle) and data points from low magnetic susceptibility
 517 (open circle). B. Opal MAR variation for the last 150 ka at Site J1007 (green) and V19-30
 518 (orange; Hayes et al., 2011). Linear sedimentation rate (LSR) for Site J1007 is shown in the
 519 bottom panel. The MIS 3 peak in opal flux is highlighted with pink shadings. The dashed arrow
 520 shows potential correlation between the Site J1007 and EEP opal MAR peak at Termination II
 521 based on benthic $\delta^{18}\text{O}$ tuning.



523 Acknowledgments

524 We would like to thank the captain and crew of the D/V *JOIDES Resolution* and JRSO for their
525 tireless efforts during the inaugural JR100 expedition. C.L., V.J.C., and Y.R. designed the
526 experiment. C.L. and V.J.C. carried out shore-based geochemical analyses, prepared figures, and
527 wrote the manuscript. S.C.B., Y.R., and L.B.C. organized and managed the expedition. J.D.W.
528 co-led shipboard stratigraphic efforts with G/B. Expedition 379T Scientists assisted in the
529 collection of G/B data and interpretation of shipboard sedimentological data. All authors
530 contributed to the interpretation of shipboard data. The expedition was funded by NSF grant
531 OCE-1756241. This study was funded by NSF grant OCE-1756241 to S.C.B. and Y.R. C.L. was
532 supported by the Chinese Scholarship Council. V.J.C. was supported by the NETL Methane
533 Hydrates Fellowship Program.

534 Open Research

535 All data used for this study are available in the supporting information (for peer review), open
536 access database, and cited references.

537
538 †**Expedition 379T Scientists (those not listed above):** Ivano W. Aiello¹, Alejandro Avila²,
539 William Biggs³, Christopher D. Charles⁴, Anson H. Cheung⁵, Kimberly deLong⁶, Isabel A. Dove⁷,
540 Xiaojing Du^{5,8}, Emily R. Estes⁹, Ursula Fuentes¹⁰, Cristina García-Lasanta¹¹, Steven L.
541 Goldstein¹², Anna Golub¹³, Julia Rieke Hagemann¹⁴, Robert G. Hatfield¹⁵, Laura L. Haynes¹⁶,
542 Anya V. Hess¹⁷, Nil Irvali¹⁸, Yael Kiro¹⁹, Minda M. Monteagudo²⁰, Jonathan E. Lambert¹²,
543 William M. Longo^{21,22}, Sarah McGrath⁵, Hailey Riechelson³, Rebecca S. Robinson⁷, John Sarao²³,
544 Adam D. Sproson²⁴, Shawn Taylor²⁵, Yusuke Yokoyama²⁶, and Siyao M. Yu¹⁷.

545
546 ¹Moss Landing Marine Laboratories, Moss Landing, California, USA. ²Center for Oceanographic
547 Research in the Eastern South Pacific (FONDAP-COPAS), University of Concepción,
548 Concepción, Chile. ³Department of Marine and Coastal Sciences, Rutgers University, New
549 Brunswick, New Jersey, USA. ⁴Scripps Institution of Oceanography, University of California, San
550 Diego, La Jolla, California, USA. ⁵Department of Earth, Environmental, and Planetary Sciences,
551 Brown University, Providence, Rhode Island, USA. ⁶Ocean Sciences Department, University of
552 California, Santa Cruz, Santa Cruz, California, USA. ⁷University of Rhode Island Graduate School
553 of Oceanography, Narragansett, Rhode Island, USA. ⁸Institute at Brown for Environment and
554 Society, Providence, Rhode Island, USA. ⁹International Ocean Discovery Program, Texas A&M

555 University, College Station, Texas, USA. ¹⁰Hydrographic and Oceanographic Services, Chilean
556 Navy, Valparaíso, Chile. ¹¹Geology Department, Western Washington University, Bellingham,
557 Washington, USA. ¹²Lamont-Doherty Earth Observatory, Columbia University, Palisades, New
558 York, USA. ¹³Department of Geology and Environmental Geoscience, Lafayette College, Easton,
559 Pennsylvania, USA. ¹⁴Department of Marine Geology and Paleontology, Alfred Wegener Institute
560 Helmholtz Center for Polar and Marine Research, Bremerhaven, Germany. ¹⁵Department of
561 Geological Sciences, University of Florida, Gainesville, Florida, USA. ¹⁶Department of Earth
562 Science and Geography, Vassar College, Poughkeepsie, New York, USA. ¹⁷Department of Earth
563 and Planetary Sciences, Rutgers University, New Brunswick, New Jersey, USA. ¹⁸Department of
564 Earth Science and Bjerknes Centre for Climate Research, University of Bergen, Bergen, Norway.
565 ¹⁹Department of Earth and Planetary Sciences, Weizmann Institute of Science, Rehovot, Israel.
566 ²⁰School of Earth and Atmospheric Sciences, Georgia Institute of Technology, Atlanta, Georgia,
567 USA. ²¹Department of Environmental Studies, Macalester College, Saint Paul, Minnesota, USA.
568 ²²Division of Environmental Health Sciences, University of Minnesota, Minneapolis, Minnesota,
569 USA. ²³College of Geosciences, Texas A&M University, College Station, Texas, USA.
570 ²⁴Biogeochemistry Research Center, JAMSTEC, Yokosuka, Japan. ²⁵Department of Geological
571 Sciences and Environmental Studies, Binghamton University, Binghamton, New York, USA.
572 ²⁶Atmosphere and Ocean Research Institute, The University of Tokyo, Chiba, Japan.

573

574 **References**

- 575 Abrantes, F., Lopes, C., Mix, A., & Pisias, N. (2007). Diatoms in Southeast Pacific surface
576 sediments reflect environmental properties. *Quaternary Science Reviews*, 26(1-2), 155-169.
577 doi:10.1016/j.quascirev.2006.02.022
- 578 Anderson, R. F., Ali, S., Bradtmiller, L. I., Nielsen, S. H., Fleisher, M. Q., Anderson, B. E., &
579 Burckle, L. H. (2009). Wind-driven upwelling in the Southern Ocean and the deglacial rise
580 in atmospheric CO₂. *Science*, 323(5920), 1443-1448. doi:10.1126/science.1167441
- 581 Antoine, D., & Morel, A. (1996). Oceanic primary production: 1. Adaptation of a spectral light-
582 photosynthesis model in view of application to satellite chlorophyll observations. *Global*
583 *Biogeochemical Cycles*, 10(1), 43-55. doi:10.1029/95GB02831
- 584 Ayers, J. M., & Strutton, P. G. (2013). Nutrient variability in Subantarctic Mode Waters forced by
585 the Southern Annular Mode and ENSO. *Geophysical Research Letters*, 40(13), 3419-3423.
586 doi:10.1002/grl.50638
- 587 Barbante, C., Barnola, J.-M., Becagli, S., Beer, J., Bigler, M., Boutron, C., . . . Chappellaz, J.
588 (2006). One-to-one coupling of glacial climate variability in Greenland and Antarctica.
589 *Nature*, 444(7116), 195-198.
- 590 Barnes, C., & Cochran, J. (1990). Uranium removal in oceanic sediments and the oceanic U
591 balance. *Earth and Planetary Science Letters*, 97(1-2), 94-101.
- 592 Bova, S.C., Rosenthal, Y., Childress, L.B., and Expedition 379T Scientists (2021), Digging Deeper
593 with the JR100: Extending high resolution paleoclimate records from the Chilean Margin to
594 the Eemian. *Pers. commun.*, <https://zenodo.org/record/5553428#.YV4q6y2cbIE>
- 595 Bradtmiller, L. I., Anderson, R. F., Fleisher, M. Q., & Burckle, L. H. (2009). Comparing glacial
596 and Holocene opal fluxes in the Pacific sector of the Southern Ocean. *Paleoceanography*,
597 24(2), n/a-n/a. doi:10.1029/2008pa001693
- 598 Brzezinski, M. A. (2002). A switch from Si(OH)₄ to NO₃-depletion in the glacial Southern Ocean.
599 *Geophysical Research Letters*, 29(12). doi:10.1029/2001gl014349

- 600 Charles, C. D., Froelich, P. N., Zibello, M. A., Mortlock, R. A., & Morley, J. J. (1991). Biogenic
601 opal in Southern Ocean sediments over the last 450,000 years: Implications for surface water
602 chemistry and circulation. *Paleoceanography*, 6(6), 697-728. doi:10.1029/91PA02477
- 603 Chase, Z., Kohfeld, K. E., & Matsumoto, K. (2015). Controls on biogenic silica burial in the
604 Southern Ocean. *Global Biogeochemical Cycles*, 29(10), 1599-1616.
605 doi:10.1002/2015gb005186
- 606 Chase, Z., McManus, J., Mix, A. C., & Muratli, J. (2014). Southern-ocean and glaciogenic
607 nutrients control diatom export production on the Chile margin. *Quaternary Science Reviews*,
608 99, 135-145. doi:10.1016/j.quascirev.2014.06.015
- 609 Clementi, V. J., & Sikes, E. L. (2019). Southwest Pacific Vertical Structure Influences on Oceanic
610 Carbon Storage Since the Last Glacial Maximum. *Paleoceanography and Paleoclimatology*,
611 34(5), 734-754. doi:10.1029/2018PA003501
- 612 Conley, D. J., & Schelske, C. L. (2001). Biogenic Silica. In J. P. Smol, H. J. B. Birks, W. M. Last,
613 R. S. Bradley, & K. Alverson (Eds.), *Tracking Environmental Change Using Lake Sediments:*
614 *Terrestrial, Algal, and Siliceous Indicators* (pp. 281-293). Dordrecht: Springer Netherlands.
- 615 de Bar, M. W., Stolwijk, D. J., McManus, J. F., Sinninghe Damsté, J. S., & Schouten, S. (2018).
616 A Late Quaternary climate record based on long-chain diol proxies from the Chilean margin.
617 *Climate of the Past*, 14(11), 1783-1803. doi:10.5194/cp-14-1783-2018
- 618 De Vleeschouwer, D., Dunlea, A. G., Auer, G., Anderson, C. H., Brumsack, H., de Loach, A., . . .
619 Jang, K. (2017). Quantifying K, U, and Th contents of marine sediments using shipboard
620 natural gamma radiation spectra measured on DV JOIDES Resolution. *Geochemistry,*
621 *Geophysics, Geosystems*, 18(3), 1053-1064.
- 622 DeMaster, D. J., 1979. The marine budgets of silica and Ph.D. Dissertation, Yale University, 308
623 pp.
- 624 Dubois, N., Kienast, M., Kienast, S., Calvert, S. E., François, R., & Anderson, R. F. (2010).
625 Sedimentary opal records in the eastern equatorial Pacific: It is not all about leakage. *Global*
626 *Biogeochemical Cycles*, 24(4), n/a-n/a. doi:10.1029/2010gb003821
- 627 Hayes, C. T., Anderson, R. F., & Fleisher, M. Q. (2011). Opal accumulation rates in the equatorial
628 Pacific and mechanisms of deglaciation. *Paleoceanography*, 26(1).
629 doi:10.1029/2010pa002008
- 630 Hebbeln, D., Lamy, F., Mohtadi, M., & Echtler, H. (2007). Tracing the impact of glacial-
631 interglacial climate variability on erosion of the southern Andes. *Geology*, 35(2).
632 doi:10.1130/g23243a.1
- 633 Hebbeln, D., Marchant, M., & Wefer, G. (2002). Paleoproductivity in the southern Peru-Chile
634 Current through the last 33 000 yr. *Marine Geology*, 186(3-4), 487-504. doi:10.1016/S0025-
635 3227(02)00331-6
- 636 Hebbeln, D., Marchant, M., Freudenthal, T., & Wefer, G. (2000). Surface sediment distribution
637 along the Chilean continental slope related to upwelling and productivity. *Marine Geology*,
638 164(3-4), 119-137. doi:10.1016/s0025-3227(99)00129-2
- 639 Henderson, G. M., & Anderson, R. F. (2003). The U-series toolbox for paleoceanography.
640 *Reviews in mineralogy and geochemistry*, 52(1), 493-531.
- 641 Heusser, L., Heusser, C., Mix, A., & McManus, J. (2006). Chilean and Southeast Pacific
642 paleoclimate variations during the last glacial cycle: directly correlated pollen and $\delta^{18}\text{O}$
643 records from ODP Site 1234. *Quaternary Science Reviews*, 25(23-24), 3404-3415.
644 doi:10.1016/j.quascirev.2006.03.011

- 645 Jouzel, J., Masson-Delmotte, V., Cattani, O., Dreyfus, G., Falourd, S., Hoffmann, G., . . . Wolff,
646 E. W. (2007). Orbital and Millennial Antarctic Climate Variability over the Past 800,000
647 Years. *Science*, 317(5839), 793. doi:10.1126/science.1141038
- 648 Kaiser, J., Lamy, F., Arz, H. W., & Hebbeln, D. (2007). Dynamics of the millennial-scale sea
649 surface temperature and Patagonian Ice Sheet fluctuations in southern Chile during the last
650 70kyr (ODP Site 1233). *Quaternary International*, 161(1), 77-89.
651 doi:10.1016/j.quaint.2006.10.024
- 652 Kienast, S. S., Kienast, M., Mix, A. C., Calvert, S. E., & François, R. (2007). Thorium-230
653 normalized particle flux and sediment focusing in the Panama Basin region during the last
654 30,000 years. *Paleoceanography*, 22(2). doi:10.1029/2006pa001357
- 655 Kuczynska, P., Jemiola-Rzeminska, M., & Strzalka, K. (2015). Photosynthetic Pigments in
656 Diatoms. *Marine Drugs*, 13(9). doi:10.3390/md13095847
- 657 Lamy, F., Hebbeln, D., & Wefer, G. (1998). Terrigenous sediment supply along the Chilean
658 continental margin: modern regional patterns of texture and composition. *Geologische*
659 *Rundschau*, 87(3), 477-494. doi:10.1007/s005310050223
- 660 Lamy, F., Kaiser, J., Ninnemann, U., Hebbeln, D., Arz, H. W., & Stoner, J. (2004). Antarctic
661 timing of surface water changes off Chile and Patagonian ice sheet response. *Science*,
662 304(5679), 1959-1962. doi:10.1126/science.1097863
- 663 Lisiecki, L. E., & Raymo, M. E. (2005). A Pliocene-Pleistocene stack of 57 globally distributed
664 benthic $\delta^{18}\text{O}$ records. *Paleoceanography*, 20(1), n/a-n/a. doi:10.1029/2004pa001071
- 665 Lopes dos Santos, R. A., Wilkins, D., De Deckker, P., & Schouten, S. (2012). Late Quaternary
666 productivity changes from offshore Southeastern Australia: A biomarker approach.
667 *Palaeogeography, Palaeoclimatology, Palaeoecology*, 363-364, 48-56.
668 doi:10.1016/j.palaeo.2012.08.013
- 669 López-Otálvaro, G.-E., Flores, J.-A., Sierro, F. J., & Cacho, I. (2008). Variations in
670 coccolithophorid production in the Eastern Equatorial Pacific at ODP Site 1240 over the last
671 seven glacial–interglacial cycles. *Marine Micropaleontology*, 69(1), 52-69.
672 doi:10.1016/j.marmicro.2007.11.009
- 673 Lougheed, B. C., & Obrochta, S. P. (2019). A Rapid, Deterministic Age-Depth Modeling Routine
674 for Geological Sequences With Inherent Depth Uncertainty. *Paleoceanography and*
675 *Paleoclimatology*, 34(1), 122-133. doi:10.1029/2018pa003457
- 676 Matsumoto, K., Sarmiento, J. L., & Brzezinski, M. A. (2002). Silicic acid leakage from the
677 Southern Ocean: A possible explanation for glacial atmospheric CO_2 . *Global*
678 *Biogeochemical Cycles*, 16(3), 5-1-5-23. doi:10.1029/2001gb001442
- 679 McManus, J., Berelson, W. M., Klinkhammer, G. P., Hammond, D. E., & Holm, C. (2005).
680 Authigenic uranium: Relationship to oxygen penetration depth and organic carbon rain.
681 *Geochimica et Cosmochimica Acta*, 69(1), 95-108. doi:10.1016/j.gca.2004.06.023
- 682 McManus, J., Berelson, W. M., Severmann, S., Poulson, R. L., Hammond, D. E., Klinkhammer,
683 G. P., & Holm, C. (2006). Molybdenum and uranium geochemistry in continental margin
684 sediments: Paleoproxy potential. *Geochimica et Cosmochimica Acta*, 70(18), 4643-4662.
685 doi:10.1016/j.gca.2006.06.1564
- 686 Mix, A. C., Rugh, W., Pisias, N. G., & Veirs, S. (1992). Color reflectance spectroscopy: A tool for
687 rapid characterization of deep-sea sediments. Paper presented at the Proceedings of the Ocean
688 Drilling Program, Part A, Initial report.

- 689 Mohtadi, M., & Hebbeln, D. (2004). Mechanisms and variations of the paleoproductivity off
690 northern Chile (24°S-33°S) during the last 40,000 years. *Paleoceanography*, 19(2), n/a-n/a.
691 doi:10.1029/2004pa001003
- 692 Mohtadi, M., Rossel, P., Lange, C. B., Pantoja, S., Böning, P., Repeta, D. J., . . . Brumsack, H.-J.
693 (2008). Deglacial pattern of circulation and marine productivity in the upwelling region off
694 central-south Chile. *Earth and Planetary Science Letters*, 272(1-2), 221-230.
695 doi:10.1016/j.epsl.2008.04.043
- 696 Mortlock, R. A., & Froelich, P. N. (1989). A simple method for the rapid determination of biogenic
697 opal in pelagic marine sediments. *Deep Sea Research Part A. Oceanographic Research*
698 *Papers*, 36(9), 1415-1426. doi:https://doi.org/10.1016/0198-0149(89)90092-7
- 699 Nederbragt, A. J., Thurrow, J. W., & Merrill, R. B. (2000). Color records from the California
700 margin: Proxy indicators for sediment composition and climatic change. *Proceedings of the*
701 *Ocean Drilling Program. Scientific results*, 167, 319-329.
- 702 Penkrot, M. L., Jaeger, J. M., Cowan, E. A., St-Onge, G., & LeVay, L. (2018). Multivariate
703 modeling of glacial-marine lithostratigraphy combining scanning XRF, multisensory core
704 properties, and CT imagery: IODP Site U1419. *Geosphere*, 14(4), 1935-1960.
- 705 Peterson, L. C., Haug, G. H., Hughen, K. A., & Röhl, U. (2000). Rapid changes in the hydrologic
706 cycle of the tropical Atlantic during the last glacial. *Science*, 290(5498), 1947-1951.
- 707 Piola, A. R., & Georgi, D. T. (1982). Circumpolar properties of Antarctic intermediate water and
708 Subantarctic Mode Water. *Deep Sea Research Part A. Oceanographic Research Papers*, 29(6),
709 687-711. doi:https://doi.org/10.1016/0198-0149(82)90002-4
- 710 Reimer, P. J., Austin, W. E. N., Bard, E., Bayliss, A., Blackwell, P. G., Bronk Ramsey, C., . . .
711 Talamo, S. (2020). The IntCal20 Northern Hemisphere Radiocarbon Age Calibration Curve
712 (0–55 cal kBP). *Radiocarbon*, 62(4), 725-757. doi:10.1017/rdc.2020.41
- 713 Reuss, N. S., Anderson, N. J., Fritz, S. C., & Simpson, G. L. (2013). Responses of microbial
714 phototrophs to late-Holocene environmental forcing of lakes in south-west Greenland.
715 *Freshwater Biology*, 58(4), 690-704. doi:10.1111/fwb.12073
- 716 Reuss, N., Conley, D. J., & Bianchi, T. S. (2005). Preservation conditions and the use of sediment
717 pigments as a tool for recent ecological reconstruction in four Northern European estuaries.
718 *Marine Chemistry*, 95(3), 283-302. doi:https://doi.org/10.1016/j.marchem.2004.10.002
- 719 Robinson, R. S., Mix, A., & Martinez, P. (2007). Southern Ocean control on the extent of
720 denitrification in the southeast Pacific over the last 70ka. *Quaternary Science Reviews*, 26(1-
721 2), 201-212. doi:10.1016/j.quascirev.2006.08.005
- 722 Romero, O. E., Kim, J.-H., & Hebbeln, D. (2017). Paleoproductivity evolution off central Chile
723 from the Last Glacial Maximum to the Early Holocene. *Quaternary Research*, 65(3), 519-
724 525. doi:10.1016/j.yqres.2005.07.003
- 725 Romero, O., & Hebbeln, D. (2003). Biogenic silica and diatom thanatocoenosis in surface
726 sediments below the Peru–Chile Current: controlling mechanisms and relationship with
727 productivity of surface waters. *Marine Micropaleontology*, 48(1), 71-90.
728 doi:https://doi.org/10.1016/S0377-8398(02)00161-5
- 729 Sallée, J.-B., Speer, K., Rintoul, S., & Wijffels, S. (2010). Southern Ocean Thermocline
730 Ventilation. *Journal of Physical Oceanography*, 40(3), 509-529. doi:10.1175/2009JPO4291.1
- 731 Sarmiento, J. L., Gruber, N., Brzezinski, M., & Dunne, J. (2004). High-latitude controls of
732 thermocline nutrients and low latitude biological productivity. *Nature*, 427(6969), 56-60.
- 733 Sigman, D. M., & Boyle, E. A. (2000). Glacial/interglacial variations in atmospheric carbon
734 dioxide. *Nature*, 407(6806), 859-869. doi:Doi 10.1038/35038000

- 735 Sloyan, B. M., & Rintoul, S. R. (2001). The Southern Ocean Limb of the Global Deep Overturning
736 Circulation*. *Journal of Physical Oceanography*, 31(1), 143-173. doi:10.1175/1520-
737 0485(2001)031<0143:Tsolot>2.0.Co;2
- 738 Stauber, J. L., & Jeffrey, S. W. (1988). PHOTOSYNTHETIC PIGMENTS IN FIFTY-ONE
739 SPECIES OF MARINE DIATOMS1. *Journal of Phycology*, 24(2), 158-172.
740 doi:10.1111/j.1529-8817.1988.tb04230.x
- 741 Strub, P. T. (1998). Coastal ocean circulation off Western South America. *The Global Coastal*
742 *Ocean. Regional Studies and Syntheses*, 273-315. Retrieved from
743 <https://ci.nii.ac.jp/naid/20001225871/en/>
- 744 Stuet, J. B. W., Marchant, M., Kaiser, J., Lamy, F., Mohtadi, M., Romero, O., & Hebbeln, D.
745 (2006). The late quaternary paleoenvironment of Chile as seen from marine archives. *Geogr.*
746 *Helv.*, 61(2), 135-151. doi:10.5194/gh-61-135-2006
- 747 Talley, L. (2013). Closure of the Global Overturning Circulation Through the Indian, Pacific, and
748 Southern Oceans: Schematics and Transports. *Oceanography*, 26(1), 80-97.
749 doi:10.5670/oceanog.2013.07
- 750 Toggweiler, J. R., Russell, J. L., & Carson, S. R. (2006). Midlatitude westerlies, atmospheric CO₂,
751 and climate change during the ice ages. *Paleoceanography*, 21(2), n/a-n/a.
752 doi:10.1029/2005pa001154
753

Figure1.

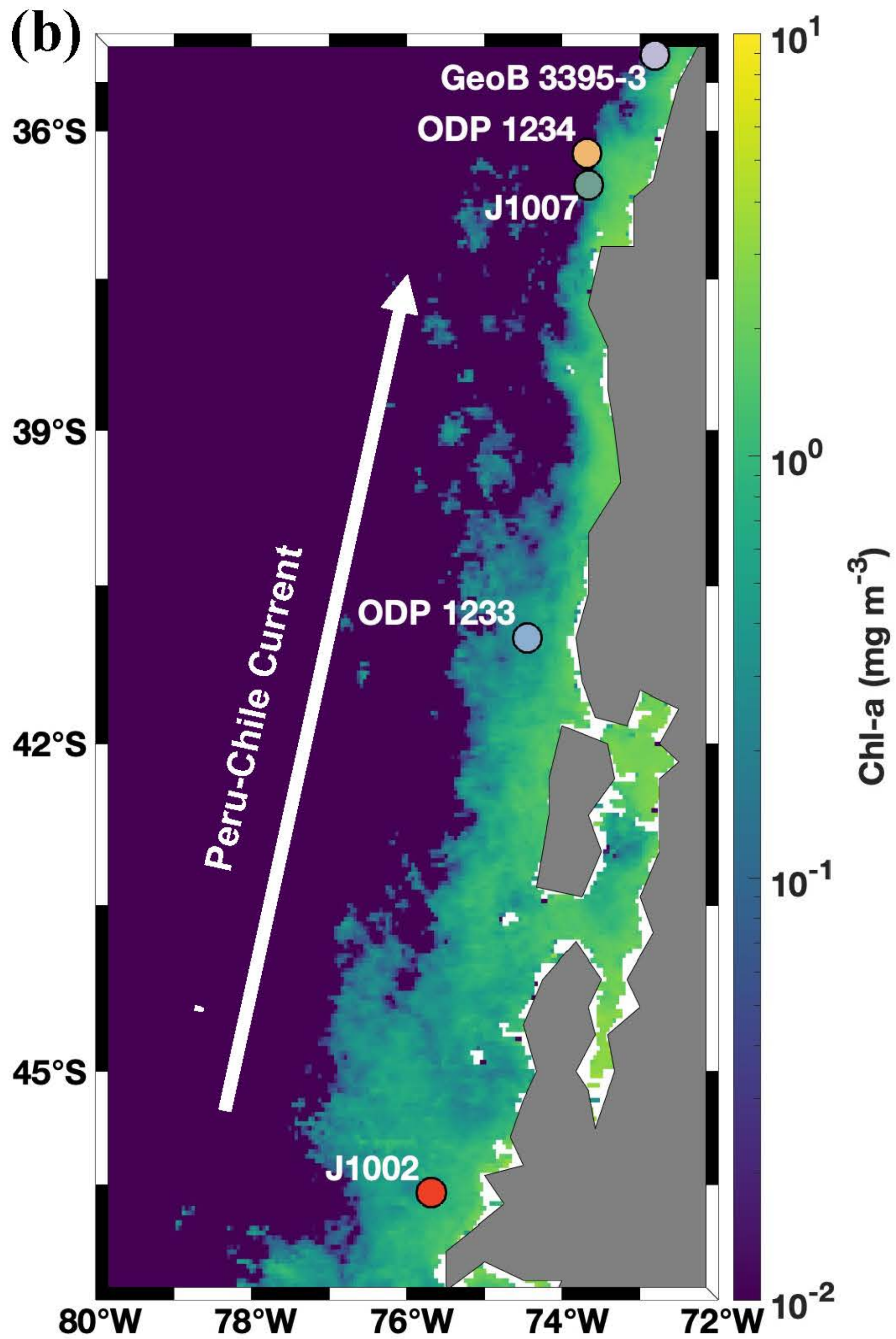
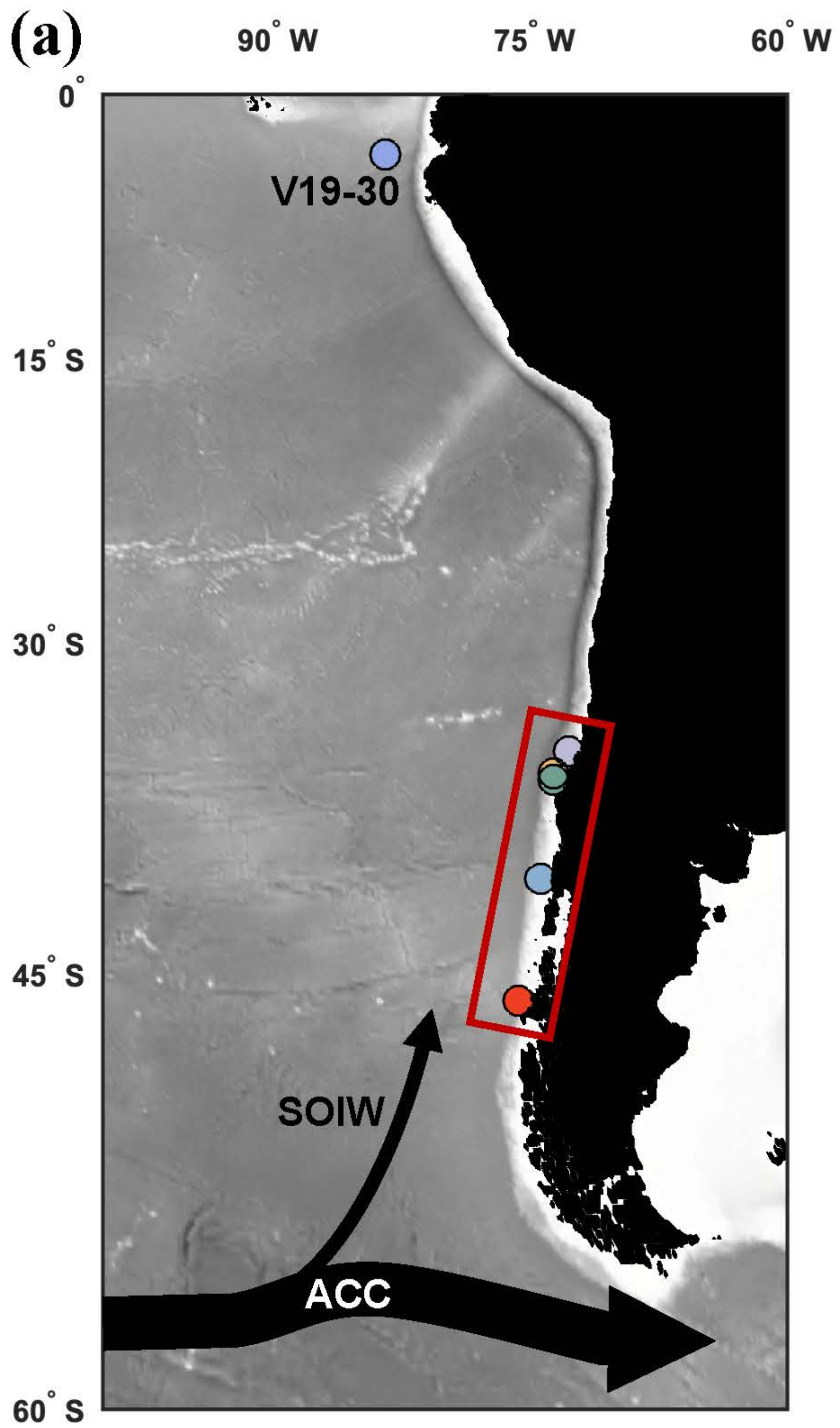


Figure2.

Figure3.

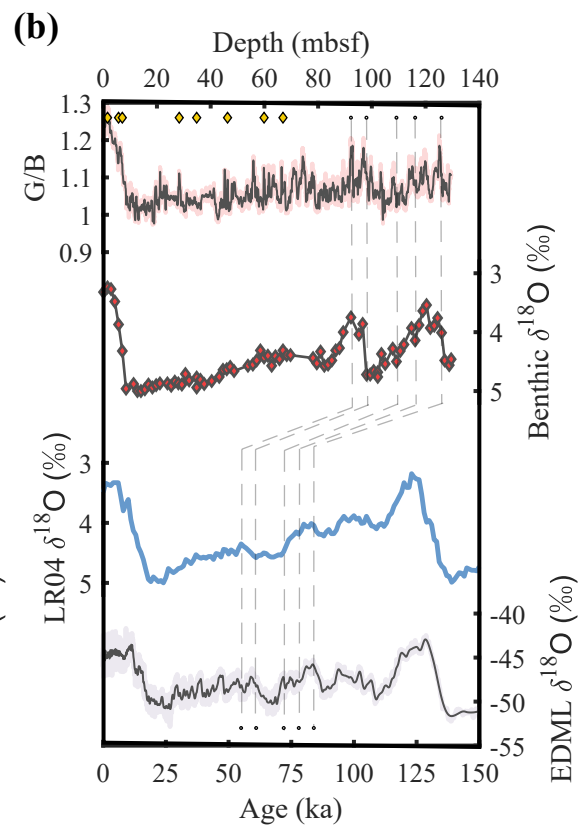
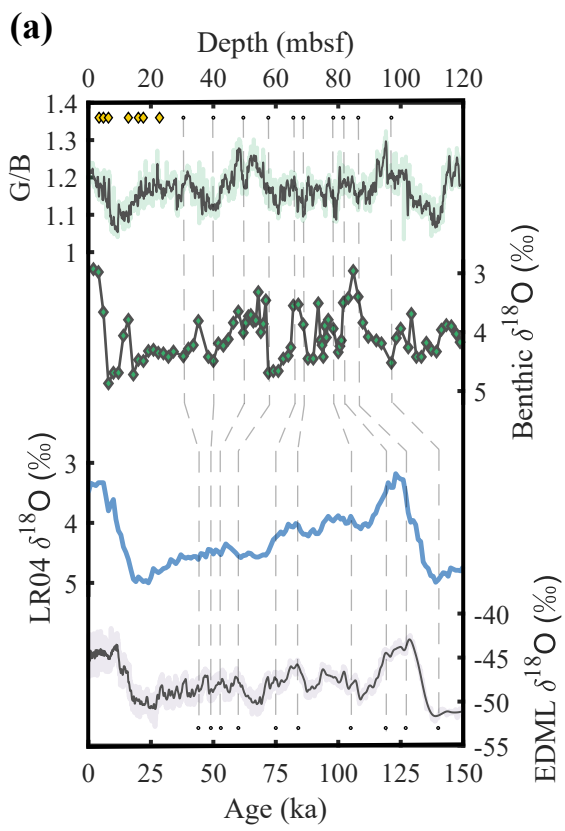


Figure4.

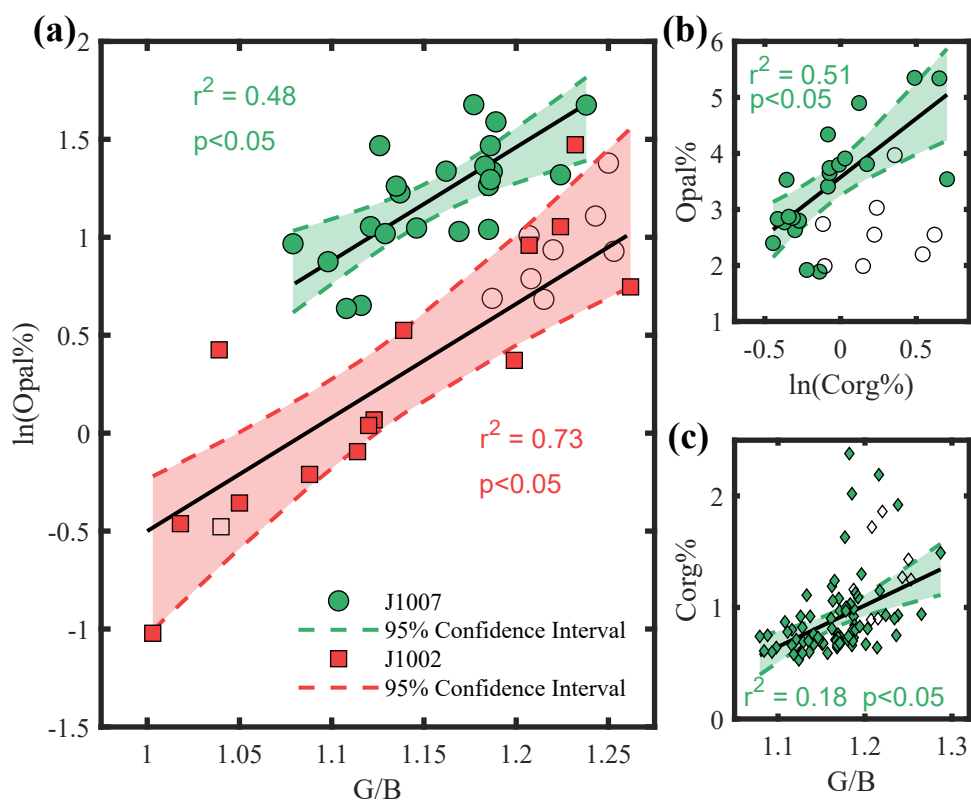


Figure 5.

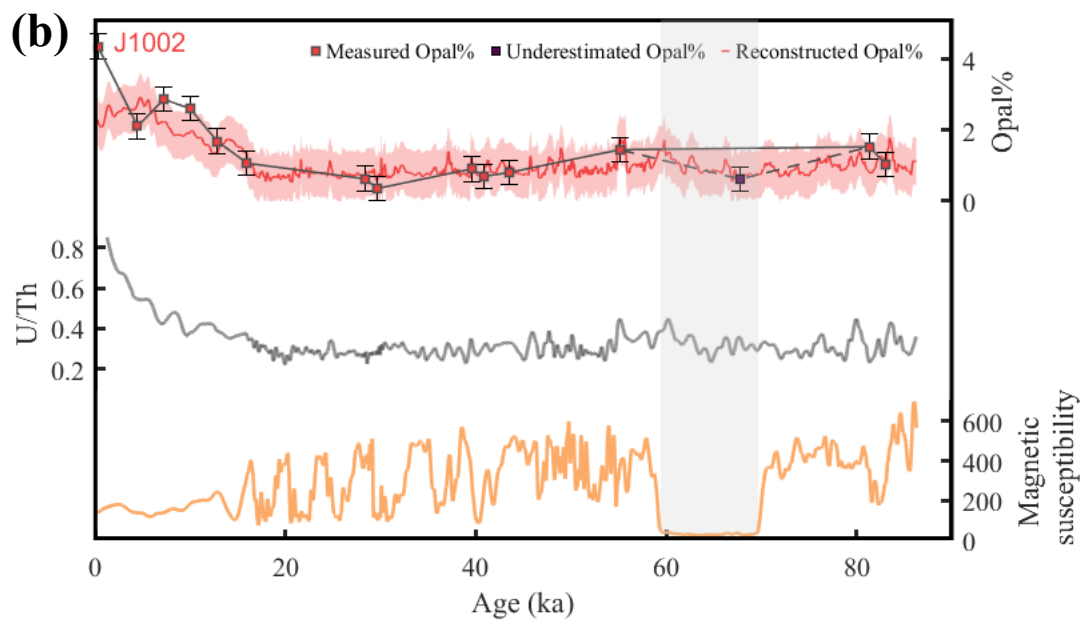
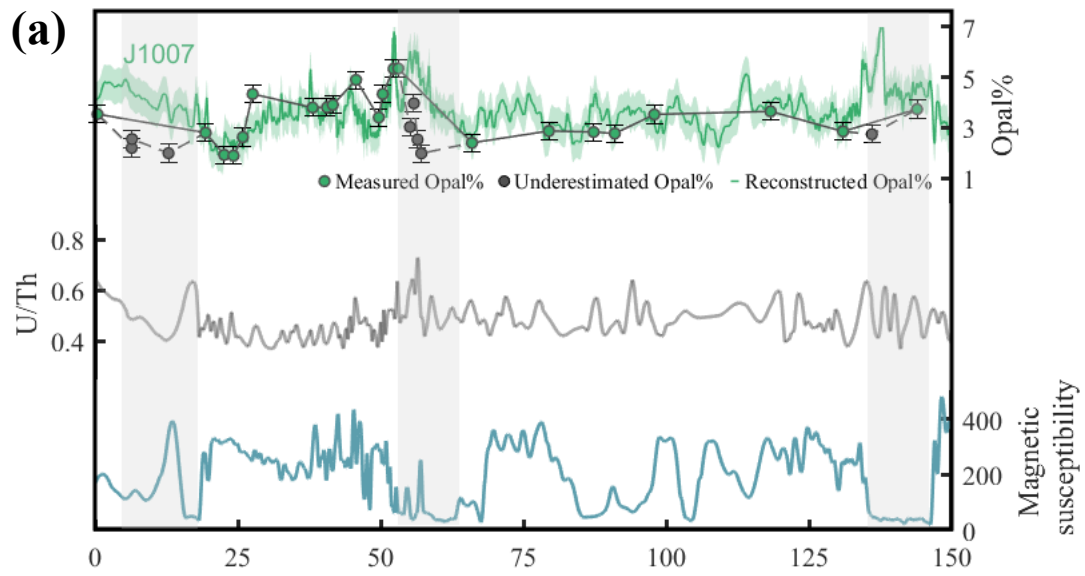


Figure6.

